



# The effects of microporosity in struts of gyroid lattice structures produced by laser powder bed fusion



A. du Plessis<sup>a,b,\*</sup>, S.M.J. Razavi<sup>c</sup>, F. Berto<sup>c</sup>

<sup>a</sup> Research group 3D Innovation, Stellenbosch University, Stellenbosch 7602, South Africa

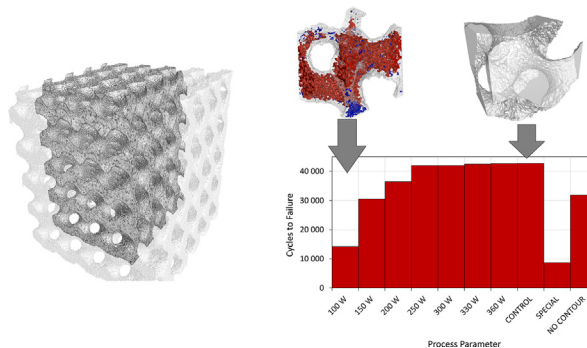
<sup>b</sup> Department of Mechanical Engineering, Nelson Mandela University, Port Elizabeth 6001, South Africa

<sup>c</sup> Department of Mechanical and Industrial Engineering, Norwegian University of Science and Technology (NTNU), Trondheim 7491, Norway

## HIGHLIGHTS

- Microporosity induced in gyroid lattice structures by process parameters
- X-ray tomography used to confirm and quantify porosity content
- Static and fatigue compression tests performed
- Both stress-relieved and hot isostatic pressed states investigated
- Effect of porosity found to be more detrimental for lack of fusion defects

## GRAPHICAL ABSTRACT



## ARTICLE INFO

### Article history:

Received 9 April 2020

Received in revised form 21 May 2020

Accepted 18 June 2020

Available online 26 June 2020

### Keywords:

Metal additive manufacturing

Laser powder bed fusion

Microporosity

Pores

Hot isostatic pressing

X-ray tomography

## ABSTRACT

Additive manufacturing by laser powder bed fusion allows the production of complex parts including lattice structures in popular metal alloys such as Ti6Al4V. Lattice structures are a class of meta-materials which hold many advantages such as the possibility for the production of lightweight parts with tailored mechanical and other properties: these have many potential applications in aerospace and medical fields. The laser powder bed fusion process can result in microporosity inside the produced material, which can affect the mechanical performance of these types of materials. In this work, different typical microporosity distributions are induced in manufactured gyroid lattice structure samples and the mechanical performance is tested by both static compression and compression-compression fatigue. X-ray tomography was used to validate the microporosity distributions and samples were tested in stress-relieved state and hot isostatic pressed state. In particular, it is found that small amounts of keyhole mode microporosity of ~0.2% make no difference while lack of fusion is critical, especially when this results in inefficient HIP pore closure. The results highlight the effect of microporosity on the mechanical performance of these materials and the results add to the knowledge base and trustworthiness of these materials.

© 2020 The Author(s). Published by Elsevier Ltd. This is an open access article under the CC BY-NC-ND license (<http://creativecommons.org/licenses/by-nc-nd/4.0/>).

## 1. Introduction

Metal additive manufacturing (AM) is fast growing in industrial applications due to the ability to manufacture components in distributed locations, with short lead times and with high part complexity [1,2]. Laser powder bed fusion (LPBF) is the AM technology that is used

\* Corresponding author at: Research group 3D Innovation, Stellenbosch University, Stellenbosch 7602, South Africa.

E-mail address: [anton2@sun.ac.za](mailto:anton2@sun.ac.za) (A. du Plessis).

most widely and allows the highest-complexity manufacturing of metal parts with typical feature sizes down to 0.1 mm in most popular metal alloys [3–5]. Despite the progress in recent years and its use in high-end applications, there are still some material quality issues and variability in the reported mechanical properties [4,6,7]. The mechanical properties are a function of microstructure, surface roughness, porosity content, residual stress and geometry of sample, which are all affected by numerous parameters during and after processing [1,8–10]. Many of these issues originate from manufacturing errors including the formation of microporosity, which can especially act as crack initiation sites in cyclic loading [11,12].

Microporosity in LPBF can be related to different underlying causes and therefore may occur in different shapes and distributions in the part. Two well-known and widely occurring types are lack of fusion and keyhole mode porosity. These are well described in [9] in the context of the major process parameters of typical LPBF systems and also discussed in some detail in a previous study of microporosity quantification using X-ray tomography of coupon cubes [13]. Some of the early identification of different porosity formation regimes in LPBF was already shown in [14]. More recently, high speed X-ray imaging has been used to observe the LPBF process and unravel the dynamics of pore formation [15,16]. One interesting result from this type of work is the finding that the keyhole cavity is present in a wider range of process parameters than previously thought [17]. Similar high speed X-ray imaging work has been conducted to image other pore formation mechanisms and continues to provide insight into the complexities of LPBF, especially when high speed imaging is combined with simulation [18].

Generally, lack of fusion porosity occurs in when the laser power is too low or the scan speed is too high, causing a single track to be narrower or shallower than expected, causing imperfect melting between adjacent tracks and subsequent layers. This type of porosity is irregular shaped and particularly detrimental to mechanical properties [11,19,20]. Keyhole mode porosity occurs when the laser power is too high or scan speed too low, causing a deep melt pool with a vapour cavity which becomes unstable creating and leaving rounded pores in the solidified material. Many variations or instabilities may occur: for example when the local melt pool temperature changes, the melt pool conditions change causing potential for porosity formation. In particular, this is correlated to porosity formation at the downward-facing regions of parts which are not supported and which have higher local temperature during processing. In fact, thermal simulation can help in identifying such conditions and analytical modelling of the porosity formation in LPBF has been widely investigated recently, see for example [21,22].

The effects of these pores on mechanical performance have been studied widely, showing that porosity at levels more than 1% typically affects mechanical performance but this varies with material type and geometry [11,23]. At porosity levels of less than 1%, static performance is typically not affected (yet exceptions may occur depending on the porosity type, shapes and locations in the part) but fatigue properties are still impacted. In this context, it has been reported that the presence of porosity has a more dramatic effect on the fatigue behaviour of AM components compared to their performance under static loading [24,25]. The main point is that porosity has a negative effect on mechanical performance and must be minimized to ensure safety. When process parameters are optimized (and porosity minimized), excellent mechanical properties comparable to the wrought material can be obtained, as shown for example for Ti6Al4V in [26,27]. This is not always the case and a wide variety of mechanical performance results have been reported in general for additive manufacturing of Ti6Al4V [28,29], for electron beam PBF in particular [30,31] and for L-PBF in particular [32].

Optimized process parameters are already well known or are developed for specific systems with specific powders. This includes the values of laser power and scan speed, coupled with the laser spot size, hatch spacing between adjacent tracks and layer height between successive layers. The scan strategy is typically a combination of zig-zag (back

and forth) hatch tracks and a contour scan track/s all around the perimeter. Process monitoring is also increasingly used to ensure a stable build process [33,34]. Finally, post-process inspection of parts is done non-destructively by X-ray tomography [35–37]. There are also well-defined stress-relief heat treatments widely used to ensure residual stresses are removed, and various post processing methods can improve the microstructure, surface quality and even the density of the parts by hot isostatic pressing (HIP) [38,39]. The HIP process has beneficial effects on fatigue performance due to microstructure homogenization and coarsening and closure of porosity as discussed in [6,40–42]. Recent work revealed the HIP efficiency of pore closure for a range of intentionally designed pores by varying LPBF process parameters, and imaged by X-ray tomography [39].

While proper parameters and inspection can ensure high quality parts suitable for critical applications, there is an interest to manufacture highly complex parts including lattice structures or topology optimized designs. The structural integrity of these more complex parts is a topic of high importance, in order to realize the full potential of metal AM and make use of the available design freedom [43].

Lattice structures are a category of complex designs allowing unique mechanical properties and functionality which can be tailored by the design and manufacturing process. They find application for medical implants where the elastic modulus is matched to the local bone elastic modulus in order to minimize stress shielding and also allow bone ingrowth into the porous structure for better long term attachment. They also find application in engineering designs where light-weighting is of interest, and have advantages in impact protection applications, amongst others. Various reviews of the design of lattice structures, their mechanical properties and their applications are available in [44–50]. Unfortunately, lattice structures often have poor mechanical properties and especially poor fatigue performance, which requires more investigation [50,51].

In this work, we investigate the structural integrity of gyroid lattice structures manufactured by LPBF in Ti6Al4V (ELI). This is done with intentionally induced differences in porosity content in the lattice struts, to reveal the effect of defects on the static and fatigue properties of these samples. In addition to variations in porosity content by controlled variations in process parameters, some samples are subjected to hot isostatic pressing (HIP). Both static and fatigue tests were undertaken and X-ray tomography used to provide insight into correlations between microporosity and the observed mechanical properties.

## 2. Methods

Lattice structure coupon samples were produced by laser powder bed fusion in Ti6Al4V (ELI) using the EOS M290 system located at Executive Engineering Pty (Ltd) near Cape Town, South Africa. Gas-atomized powder used was EOS-supplied Ti6Al4V (ELI) with typical spherical morphology reported as having D90 size of 50.0  $\mu\text{m}$ . The chamber is filled with argon and flowed across the build platform during processing as is default for this system. The baseplate of Ti6Al4V is default 250×250×25 mm.

The gyroid lattice design was selected due to its impressive manufacturability and lack of sharp corners which should enhance its fatigue properties (lack of stress concentrations typical in corners). For this work, a design density of 50% was used in order to obtain reasonable wall thickness. A total of five unit cells of 3 mm in each direction was selected to produce a total cube sample size of 15 mm, with a wall thickness of 1.2 mm. Using smaller unit cells or lower density would have resulted in thinner walls, complicating the manufacturability and resulting in potentially poor mechanical results as shown in recent studies with walls and struts below 1 mm [52,53].

In this work, the effect of defects (microporosity) was the primary topic of interest, which necessitated wall thickness > 1 mm. At this thickness, multiple adjacent laser scanning tracks are used to manufacture the sample, resulting in good quality production. In similar recent

work on gyroid sheet-based designs manufactured in Ti6Al4V [54], it was clearly shown and discussed how thin gyroid sheets consisted of only one scan track in places. Their work mentions the potential for pore formation at the overlap between hatch and contour tracks, something that has been discussed in the previous work [13] but was not present in this work. Other differences include the stress-relief heat treatment used here, which eliminates residual stress.

The total sample number was limited by the available mechanical test facilities and cost to produce samples. In this work, the internal porosity inside the strut material is referred to as microporosity, different from the designed macro-porosity between struts. Microporosity percentage is thus calculated as relative to material volume as usual for bulk materials.

X-ray tomography was used extensively in this work, a review of the use of this technique in additive manufacturing is found in [35]. Scans were performed with a GE Nanotom S system. Full samples were scanned at 14  $\mu\text{m}$  voxel size, using 150 kV and 130  $\mu\text{A}$ , with 0.5 mm copper beam filter, and 3000 images in a full rotation. Close-up scans of tips of the samples were performed at 3.75  $\mu\text{m}$  (with a reduced field of view), for improved quantification of the homogenous porosity distributions intentionally created. These scans were performed with 140 kV and 20  $\mu\text{A}$ , without beam filter and with 2800 images in a full rotation of the sample. All analysis from microCT data was performed by the software Volume Graphics VGSTUDIO MAX 3.3. Porosity quantification was performed according to the same procedure as in previous work [55] using in this case a selected region of interest to minimize image artefact error (near edges). To minimize human bias in thresholding, this procedure uses a threshold which is selected manually as usual, but this is followed by an automatic local refinement of the threshold based on the local grey values up to 4 voxels on either side of the initial threshold, across the entire volume. This allows for an improved (sub-voxel interpolation based) segmentation despite possible variations of brightness across the image and despite some possible human error in initial selection. This is used directly as input for porosity quantification, not relying on any further defect detection algorithms.

An initial characterization of the important features of the produced lattice is given in Fig. 1. X-ray tomography data is presented in the form of a 3D surface rendering in Fig. 1(a) and a cross-sectional slice image in 1(b). The slice image clearly shows the formation of microporosity inside the gyroid walls in this case. Fig. 1(c) shows a wall thickness analysis which indicates the majority of the structure has a constant wall thickness of 1.2 mm. Fig. 1(d) shows a nominal-actual comparison which highlights deviations from the nominal CAD design. In this "frontal" 3D view it is clear that some excess material is found at the downward facing regions ("down-skin") as seen in red. A video and close-up image of this are provided as supplementary material.

The sample shown in Fig. 1 was measured as  $14.7 \times 14.7 \times 14.8$  mm, with an actual density of 49% (the design was  $15 \times 15 \times 15$  mm and 50% density). Small differences between design and actual produced sample are expected, and are system-specific – likely in this case due to layer slicing and scan strategy. Local variations show excess material at downward facing areas as seen in Fig. 1(d). Samples were produced with a variety of process parameters, in a similar process as done recently for small cubes in [13]. The nominal/suggested process parameters for Ti6Al4V at 1200 mm/s and 280 W produced no observed porosity at the resolution of the microCT scan of the whole sample, therefore high resolution scans of the tips of the samples were performed additionally for quantification. These high resolution scans of 3.75  $\mu\text{m}$  were performed with the Nanotom S system using scan parameters 140 kV and 20  $\mu\text{A}$ .

Samples were produced with default prescribed parameters for Ti6Al4V on the EOS M290 system – these are 280 W, 1200 mm/s scan speed, 0.14 mm hatch spacing, 0.03 mm layer height and hatch scanning in zig-zag formation with 67 degree rotation on each layer. Contour scanning is performed after the hatching on each layer as per default

on the system. Variations of these parameters were implemented to intentionally manufacture samples with lack of fusion pores as well as keyhole pores, by varying the power only over the range of power settings from 100 W to 360 W (all other parameters including scan speed fixed). In addition, one porous case was produced using custom settings (termed "special") – this setting was custom developed for medical implant use and details may not be shared, but usually this is meant for much thinner lattices and might therefore be optimized on contours and not inner hatch. A final case was investigated with no contour track scanning – the contour tracks presumably improve the surface roughness and it was of interest to include this case without contours for comparison (inner hatch parameters identical to control samples). In total 10 different process parameters were used, with four samples of each used in this study, totalling 40 samples.

The energy density parameter is often reported in order to facilitate comparison between different LPBF studies. This parameter has some serious limitations as described in [56] and must be used with care. We nevertheless report that at 360 W (our highest power used), the energy density in our case was 67 J/mm<sup>3</sup> and in this case we find approximately 0.2% keyhole mode porosity.

Samples were all subjected to stress-relief heat treatment (650 degrees in argon for 3 h) prior to cutting from the baseplate. One sample of each process parameter was subjected to quasi-static compression test under a displacement rate of 0.3 mm/min and one of each to fatigue test using an MTS landmark servohydraulic test machine (Minnesota, USA) with a load cell capacity of 50 kN. Uniaxial fatigue tests were performed under load control with a frequency of 20 Hz and a loading ratio of 0.1. The maximum fatigue stress was set to 70% of the static compressive strength. The load-displacement data was directly recorded from the test machine during static tests and the number of cycles to failure was recorded in fatigue tests, selecting a reduction of elastic modulus by 2% as failure.

Two of each process parameter type was subjected to hot isostatic pressing (HIP) followed by static and fatigue test similar to above. HIP was performed at Kitty Hawk Products Inc. (USA) according to the routine aerospace standard cycle for Ti6Al4V – typically 920 °C at 100 MPa and 2 h hold time. The same cycle was used in a prior study of porosity changes in Ti6Al4V produced by LPBF – showing the same variation of pore distribution and showing efficient pore closure for the settings above 120 W [39] There was a complication to the samples subjected to HIP, in that the sample numbers were not visible after HIP. The tests conducted on stress-relieved samples is summarized in Table 1 and the samples intended for HIP were according to the same test matrix. All 20 samples from HIP (10 for static and 10 for fatigue test) were microCT scanned to measure their porosity and a random selection of samples was made for static and fatigue tests. Only four samples showed porosity in microCT scans so these were used for fatigue tests, to better identify the effect of pores on the fatigue life despite the improved ductility of the bulk material.

### 3. Results and discussion

#### 3.1. Stress-relieved samples

MicroCT scans of tips of samples in stress-relieved state were done for each process parameter set, with microporosity quantified in each case. Initial scans of the entire lattice cube (as in Fig. 1) did not allow detailed inspection of the microporosity due to resolution limits, which prompted additional scans of the tips of samples at a higher resolution. In Fig. 2 a representative microCT slice image (cross sectional image) is shown for each process parameter, with square regions of interest used for quantification (seen by contrast enhancement). The cubic regions selected for analysis were selected in the middle of strut material to minimize edge errors due to beam hardening (an image artefact). These results follow the same trend as a previous study of 5 mm cubes of the same material produced with the same process parameters

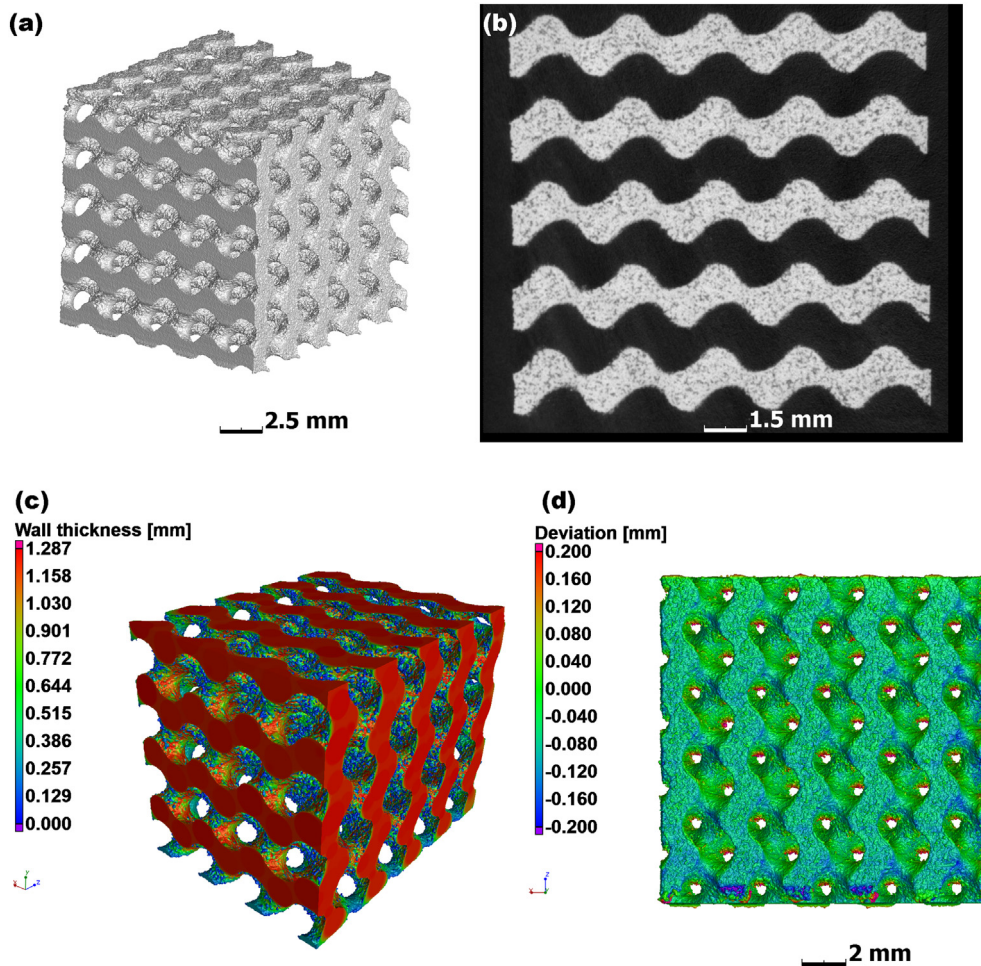


**Fig. 1.** Characterization of gyroid lattices by X-ray tomography: (a) 3D surface rendering, (b) cross sectional slice image showing presence of microporosity, (c) thickness analysis showing 1.2 mm wall thickness even across the structure, (d) deviation from design showing most of part within 0.05 mm with some droop formation on down-skin surfaces (red indicates positive deviation from design up to 0.2 mm). A supplementary video is provided for visualization of (d).

**Table 1**

Test matrix for static compression tests (1 sample of each = 20 samples total).

Process parameter	Stress-relieved	HIP
100 W	Yes	Yes
150 W	Yes	Yes
200 W	Yes	Yes
250 W	Yes	Yes
300 W	Yes	Yes
330 W	Yes	Yes
360 W	Yes	Yes
Control (280 W)	Yes	Yes
Special	Yes	Yes
No-contour	Yes	Yes

and reported in [55] in more detail. At laser power of 100 W, lack of fusion is excessive and clearly visible in the image with microporosity more than 15%. At 150 W only small pores are seen with a value of 1.7% randomly distributed. At 200 W, 250 W and 300 W, no pores are detected. At 330 and 360 W, small isolated and rounded pores are visible which can be related to keyhole porosity at levels of only 0.05% and 0.18% respectively. The samples produced with special parameters are clearly highly porous with a porosity value of 26.3%, with unmelted particles seen in the images and larger cavities present, likely due to

unmelted regions. The final “no contour” sample does not contain microporosity. This is not surprising, as the lack of contour scanning is expected to influence only the surface and not the internal microporosity.

Static compression tests were conducted at a displacement rate of 0.3 mm/min and failure load and deformation at failure recorded. Fig. 3 illustrates the compressive strengths of the tested lattice samples. As shown in Fig. 3, the samples with high levels of porosity (100 W and special case) had very poor compressive strengths while increasing quality (with less microporosity) resulted in higher compressive strength. Interesting is that the highest compressive strength was in the case of 360 W including spherical keyhole pores at a level of approximately 0.2%. Finally, it is also interesting to observe the sample lacking contour tracks has a slightly lower compressive strength – confirming experimentally the surface roughness does indeed affect the static strength properties for these structures.

Compression-compression fatigue tests were conducted at a load ratio of 0.1 using the maximum stress at 70% of the compressive strength obtained from static compression tests in each case. In Fig. 4 the cycles to failure are shown for each of these process parameter sets. Poorest results are found for the most porous samples as expected, with the “special” case having the shortest fatigue life. As the density increases (microporosity decreases), the cycles to failure increases even up to the high power region including keyhole pores. The presence of keyhole pores at levels approximately up to 0.2% as here does not seem to negatively influence the fatigue life. The “no-contour” sample

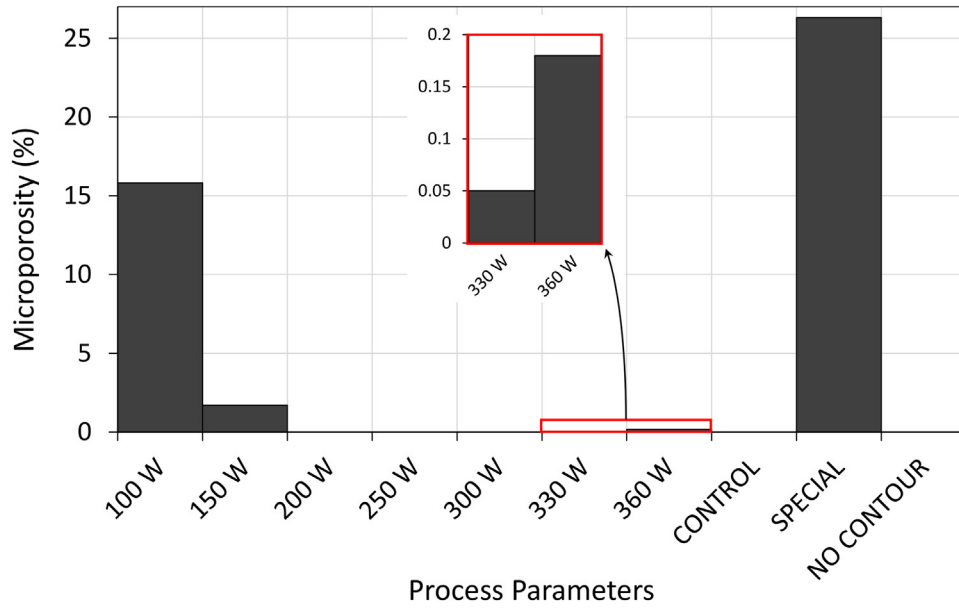
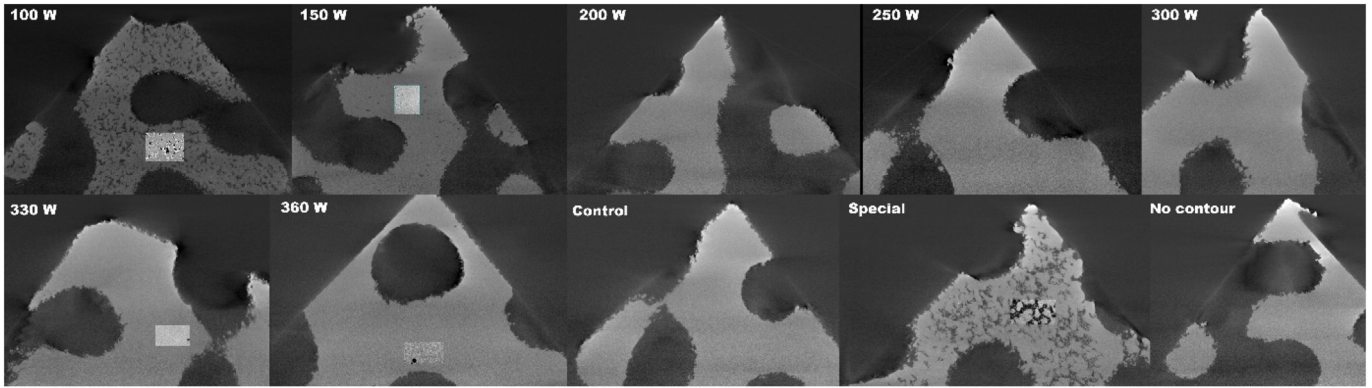


Fig. 2. High resolution microCT scans and microporosity values for each process parameter type. Lack of fusion pores at low power (e.g. 100 W) are irregular shaped, while keyhole pores at high power (e.g. 360 W) are rounded.

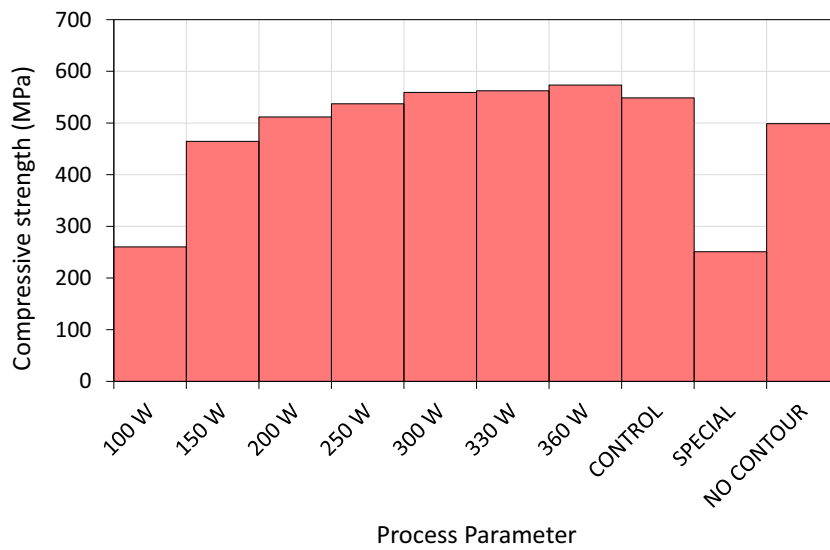


Fig. 3. Compressive strength at each process parameter set.

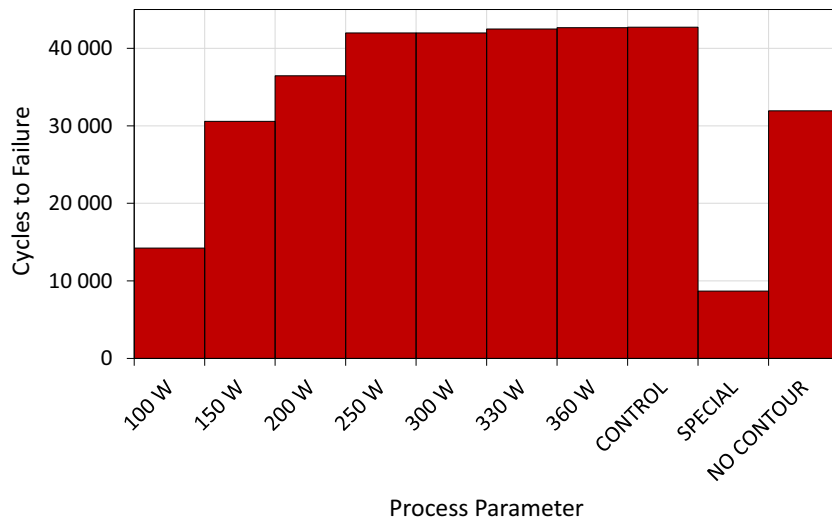


Fig. 4. Fatigue life for each parameter set at 70% of the compressive strength in each case (e.g. 384 MPa for control sample).

shows lower number of cycles to failure, indicating the positive contribution of contouring tracks on the fatigue life. This is presumably due to rougher surface of contourless samples with higher number of crack initiation locations.

The summary of all mechanical test results for stress-relieved samples is provided in Tables 2 and 3. Additional information such as the strain at failure and specific max stress in each fatigue test is included in the Tables. Only one sample of each was tested due to the large differences in porosity content. The microporosity measured from the tips of each sample is also included.

### 3.2. Hot isostatic pressed samples

Samples were subjected to hot isostatic pressing (HIP) according to standard procedure for Ti6Al4V, with the aim to close the microporosity and improve the ductility of the material. This was done in order to investigate the effect of these improvements on the mechanical performance of the gyroid samples for a direct comparison with the stress-relieved samples. HIP is often used to improve the performance of AM parts which prompted this investigation. One sample of each state was destined for static and fatigue tests totalling 20 samples subjected to HIP. All sample labels disappeared during the HIP process presumably due to the high temperature, which complicated the analysis. However, microCT was used to analyze the remaining porosity which was effectively zero for 16 out of 20 samples. Fig. 5 shows high resolution scans of the tips of samples after HIP, one example of each with and without porosity. The inefficient pore closure of four samples is explained as

Table 2

Static loading test results for stress-relieved samples.

Description	Microporosity (%)	Compressive strength (MPa)	Strain at failure [(%)
100 W	15.8	260	9.43
150 W	1.7	464	13.99
200 W	0	512	11.77
250 W	0	537	12.71
300 W	0	559	12.48
330 W	0.05	562	11.64
360 W	0.18	573	11.50
Control	0	549	12.63
Special	26.3	251	9.82
No contour	0	499	11.82

Table 3

Fatigue test results for stress-relieved samples.

Description	Microporosity (%)	Max stress (MPa)	Fatigue life
100 W	15.8	182	14,227
150 W	1.7	325	30,568
200 W	0	358	36,443
250 W	0	376	41,985
300 W	0	391	41,975
330 W	0.05	394	42,488
360 W	0.18	401	42,671
Control	0	384	42,726
Special	26.8	176	8,686
No contour	0	349	31,937

the cases with initially high porosity (100 W and special parameters cases) of which two of each were subjected to HIP. Presumably, the high interconnectivity and high porosity ensured gas penetrated the cavities and did not close these pores, as reported in [39].

Since samples were randomly selected for mechanical tests, no direct correlation is possible, but it is known that four of 20 samples had porosity in excess of 15% while pores were closed in all others. Observing the static test results in Table 4, all compressive strengths are lower than the control value of stress-relieved samples, and strain at failure is higher. This can be explained by the improved ductility of the material due to the HIP process. The details of fatigue test data are given in Fig. 6 and Table 5. Four samples showed extremely low number of cycles to failure while the other six all had very high fatigue life. It is highly likely that the four early failures are due to inefficient HIP of the four samples resulting in residual internal porosity (e.g. Fig. 5(b)).

### 3.3. Failure modes

All stress-relieved samples failed in a clear diagonal shear pattern under static compression as in Fig. 7(a). Samples subjected to HIP also show crack formation along a diagonal pattern but the cracks are smaller and vertically oriented as shown in Fig. 7(b). Stress-relieved samples show some discolouration which can indicate surface oxidation either during LPBF or during the stress relief cycle. This can affect the mechanical properties, reducing the ductility of the material. All samples were subjected to the same stress relief cycle, including the samples subjected to HIP subsequently.

Fatigue failure occurred for both stress-relieved and HIP samples as in Fig. 8, with vertically oriented cracks mainly along diagonal regions.

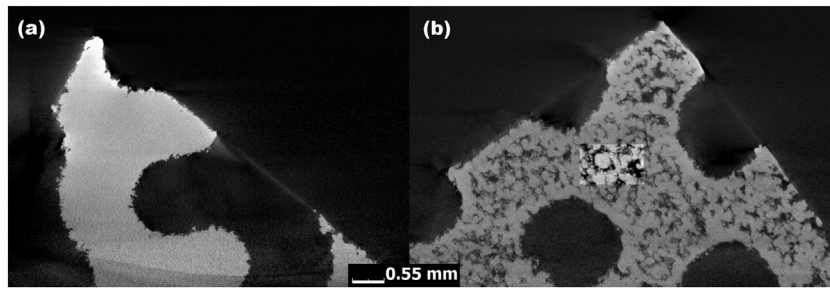


Fig. 5. Evidence of (a) efficient pore closure observed in 16 samples, and (b) inefficient pore closure due to highly connected microporosity in four samples.

Table 4

Static load test results for 10 samples after HIP.

Compressive strength (MPa)	Strain at failure (mm)
469	21.95
504	22.19
537	21.31
479	21.47
515	20.00
506	25.58
545	21.46
433	19.01
515	20.95
436	24.03

Table 5

Fatigue test results for 10 samples after HIP, at fixed maximum stress of 278 MPa.

Porosity	Cycles to failure
Yes	269
Yes	427
Yes	273
Yes	241
No	201,170
No	560,255
No	253,308
No	874,820
No	656,180
No	601,430

#### 4. Discussion

A number of interesting results are revealed by these experiments. Firstly, there are clear effects of microporosity on the mechanical performance of the gyroid lattice structures in stress-relieved state. The lack-of-fusion porosity causes reduced static compression strength and lower fatigue life for stress-relieved samples, with increasing compressive strength and fatigue life for increasing power (and less lack of fusion). The keyhole mode porosity, while only in low amounts, does not seem to affect the compressive strength or the fatigue life at all, which is an interesting result. This means that the safe processing window is shifted towards higher power: even when some keyhole porosity is present, the mechanical performance is acceptable. This might be due to microstructure changes as the power increases – more remelting occurs and finer microstructure is produced in the as-built state with increased power. The “special” case of modified process parameters clearly results in lack-of-fusion porosity and results are similar to the case for 100 W (excessive lack of fusion) with low strength

and low fatigue life. Similar results were reported for sheet-based gyroid lattice samples with some porosity differences related to contour-hatch overlap in [54]. The “no-contour” sample shows slightly reduced strength and fatigue life, despite the lack of porosity. This highlights the importance of both surface quality and microporosity in mechanical performance [42].

The samples that were subjected to HIP showed improved ductility and slightly reduced strength in static compression, compared to the stress-relieved samples. This is consistent with the coarsening of the microstructure and shown for bulk Ti6Al4V [6,42]. The coarsening of the microstructure improves the ductility and slightly reduces the strength as also shown in [57]. The failure mode is different in HIP samples, with small cracks located along diagonals, in contrast to the fully diagonal shear observed in stress-relieved state. Due to higher ductility of the HIP samples, uniform deformation of the cubic samples with increased lateral dimensions was evident (see Figs. 7 and 8). On the other hand, stress relieved samples represented a sudden brittle type of failure with lower strain at failure. Fatigue tests showed four cases of very

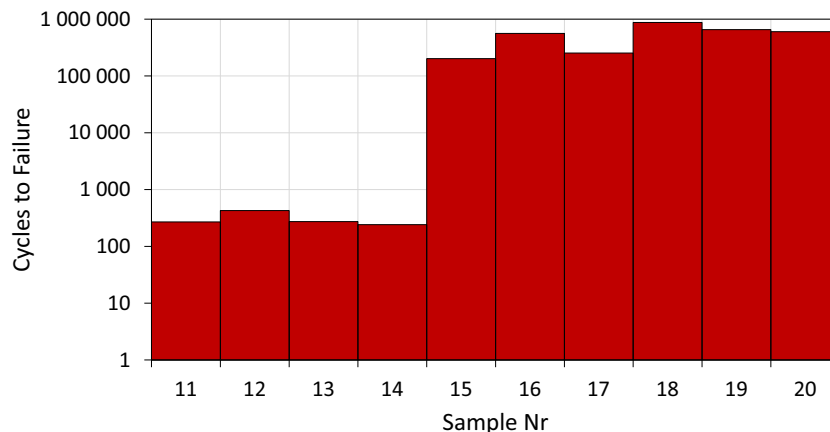
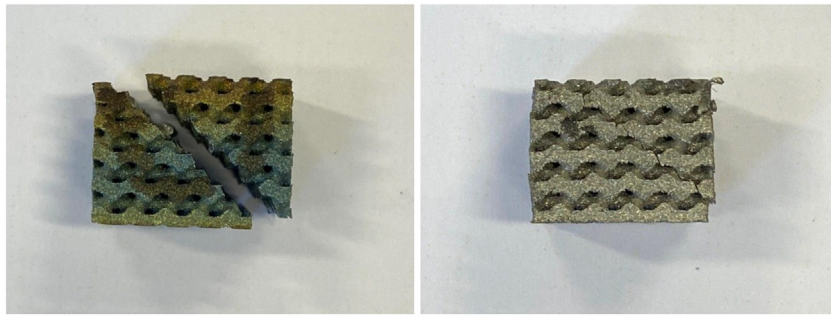
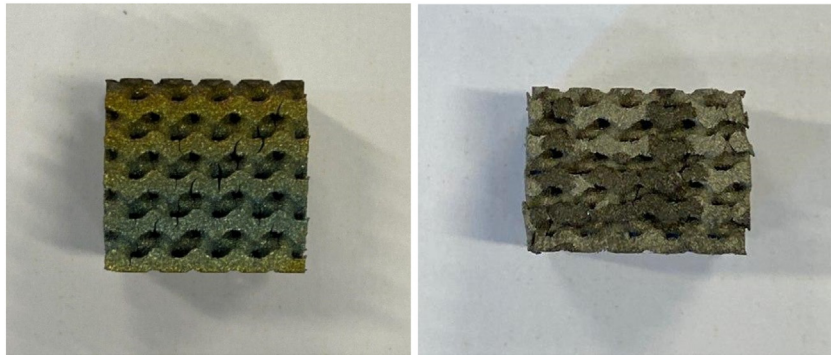


Fig. 6. Fatigue life of 10 samples at fixed maximum stress of 278 MPa.



**Fig. 7.** Static compression failure modes: (a) stress-relieved samples, (b) HIP samples. Scale: cube width is 15 mm.



**Fig. 8.** Fatigue failure modes: (a) stress-relieved samples, (b) HIP samples. Scale: cube width is 15 mm.

low life which could be correlated with the highly porous samples after HIP (100 W and special case) – due to highly interconnected porosity open to the surface, the HIP process was ineffective for these samples. The equivalent stress-relieved samples have compressive strengths of ~250 MPa. At a fixed maximum fatigue load for these samples, the short life is to be expected. In the case of the other six samples with high density in struts, all fatigue lives were high. This higher fatigue lives compared to the samples with stress-relieved condition is related to two factors namely the microstructural evolution and reduced amount of porosity. The elevated temperature during the HIP process increases the ductility, making the material more resistant against cyclic loadings. Additionally, the lower amount of internal defects in HIP samples lower the stress concentrations and consequently results in a less critical stress state in the struts. These varied from 200,000 to 900,000 cycles, which shows that despite porosity being zero in all cases, there is still a wide spread of results. Despite not being directly comparable, this is consistent with results reported for sheet-based gyroid lattices subjected to 60% load cycles in compression fatigue [58]. Since these samples presumably have the same microstructure and lack of pores, the variability in fatigue life can be explained by the surface roughness only. It might be that surface quality is a factor in differences between these samples as cracks can initiate on the surface and this was studied in some detail in recent work for cylindrical lattice struts [59]. The presence of vertical cracks might indicate the cracks initiate in the rough downskin (downward-facing) surface.

## 5. Conclusions

The reported experimental data improves our understanding of the mechanical performance of lattice structures produced by laser powder bed fusion. The role of microporosity is related to the performance of stress-relieved samples, showing that high density (lack of microporosity in struts) is important for strength and fatigue life, but keyhole porosity is not critical at the low levels investigated. This has

implications for using a wider processing window, with some levels of keyhole porosity being acceptable. The negative effect of the surface roughness by lack of contour track scanning is shown to cause reduction in strength and fatigue life, in the absence of any other differences between control and no-contour samples. This effect presumably becomes more important as the relative surface area increases for different lattice designs and warrants more detailed investigation, especially as lattices typically contain large surface areas, and surface modification might be crucial for improved performance.

The HIP of lattices with different porosity distributions results in slightly reduced strength and higher ductility as expected, but some samples show pores are not closed by HIP with resulting very poor fatigue life. Nevertheless, the fully densified samples subjected to HIP all show very high fatigue life considering the high loads used. The results reported here are promising and motivate further studies to improve the performance of lattice structures produced by laser powder bed fusion.

Supplementary data to this article can be found online at <https://doi.org/10.1016/j.matdes.2020.108899>.

## Data availability statement

Data is available on request.

## Declaration of Competing Interest

The authors declare no conflict of interest in this work.

## Acknowledgements

The Collaborative Program for Additive Manufacturing (CPAM), funded by the South African Department of Science and technology, is acknowledged for financial support.

## References

- [1] T. Debroy, H.L. Wei, J.S. Zuback, T. Mukherjee, J.W. Elmer, J.O. Milewski, A.M. Beese, A. Wilson-Heid, A. De, W. Zhang, Additive manufacturing of metallic components – process, structure and properties, *Prog. Mater. Sci.* 92 (2018) 112–224, <https://doi.org/10.1016/j.pmatsci.2017.10.001>.
- [2] T. DebRoy, T. Mukherjee, J.O. Milewski, J.W. Elmer, B. Ribic, J.J. Blecher, W. Zhang, Scientific, technological and economic issues in metal printing and their solutions, *Nat. Mater.* (2019) 1, <https://doi.org/10.1038/s41563-019-0408-2>.
- [3] C.Y. Yap, C.K. Chua, Z.L. Dong, Z.H. Liu, D.Q. Zhang, L.E. Loh, S.L. Sing, Review of selective laser melting: materials and applications, *Appl. Phys. Rev.* 2 (2015), 041101, <https://doi.org/10.1063/1.4935926>.
- [4] J.J. Lewandowski, M. Seifi, Metal additive manufacturing: a review of mechanical properties, *Annu. Rev. Mater. Res.* 46 (2016) 151–186, <https://doi.org/10.1146/annurev-matsci-070115-032024>.
- [5] D. Bourell, J.P. Kruth, M. Leu, G. Levy, D. Rosen, A.M. Beese, A. Clare, Materials for additive manufacturing, *CIRP Ann.* 66 (2017) 659–681, <https://doi.org/10.1016/j.cirp.2017.05.009>.
- [6] M. Seifi, A. Salem, J. Beuth, O. Harrysson, J.J. Lewandowski, Overview of materials qualification needs for metal additive manufacturing, *JOM* 68 (2016) 747–764, <https://doi.org/10.1007/s11837-015-1810-0>.
- [7] M. Seifi, M. Gorelik, J. Waller, N. Hrabe, N. Shamsaei, S. Daniewicz, J.J. Lewandowski, Progress towards metal additive manufacturing standardization to support qualification and certification, *JOM* 69 (2017) 439–455, <https://doi.org/10.1007/s11837-017-2265-2>.
- [8] A. Yadollahi, M.J. Mahtabi, A. Khalili, H.R. Doude, J.C. Newman, Fatigue life prediction of additively manufactured material: effects of surface roughness, defect size, and shape, *Fatigue Fract. Eng. Mater. Struct.* 41 (2018) 1602–1614, <https://doi.org/10.1111/ffe.12799>.
- [9] J.P. Oliveira, A. LaLonde, J. Ma, Processing parameters in laser powder bed fusion metal additive manufacturing, *Mater. Des.* (2020), 108762, <https://doi.org/10.1016/j.matdes.2020.108762>.
- [10] J.P. Oliveira, T.G. Santos, R.M. Miranda, Revisiting fundamental welding concepts to improve additive manufacturing: from theory to practice, *Prog. Mater. Sci.* 107 (2020), 100590, <https://doi.org/10.1016/j.pmatsci.2019.100590>.
- [11] A. du Plessis, I. Yadroitsava, I. Yadroitsev, Effects of defects on mechanical properties in metal additive manufacturing: a review focusing on X-ray tomography insights, *Mater. Des.* 187 (2020) <https://doi.org/10.1016/j.matdes.2019.108385>.
- [12] S.M.J. Razavi, P. Ferro, F. Berto, J. Torgersen, Fatigue strength of blunt V-notched specimens produced by selective laser melting of Ti-6Al-4V, *Theor. Appl. Fract. Mech.* 97 (2018) 376–384, <https://doi.org/10.1016/j.tafmec.2017.06.021>.
- [13] A. du Plessis, Effects of process parameters on porosity in laser powder bed fusion revealed by X-ray tomography, *Addit. Manuf.* 30 (2019) <https://doi.org/10.1016/j.addma.2019.100871>.
- [14] H. Gong, K. Rafi, H. Gu, T. Starr, B. Stucker, Analysis of defect generation in Ti-6Al-4V parts made using powder bed fusion additive manufacturing processes, *Addit. Manuf.* 1 (2014) 87–98, <https://doi.org/10.1016/j.addma.2014.08.002>.
- [15] A.A. Martin, N.P. Calta, S.A. Khairallah, J. Wang, P.J. Depond, A.Y. Fong, V. Thampy, G.M. Guss, A.M. Kiss, K.H. Stone, C.J. Tassone, J. Nelson Weker, M.F. Toney, T. van Buuren, M.J. Matthews, Dynamics of pore formation during laser powder bed fusion additive manufacturing, *Nat. Commun.* 10 (2019) 1–10, <https://doi.org/10.1038/s41467-019-10009-2>.
- [16] C.L.A. Leung, S. Marussi, R.C. Atwood, M. Towrie, P.J. Withers, P.D. Lee, In situ X-ray imaging of defect and molten pool dynamics in laser additive manufacturing, *Nat. Commun.* 9 (2018) 1–9, <https://doi.org/10.1038/s41467-018-03734-7>.
- [17] R. Cunningham, C. Zhao, N. Parab, C. Kantzos, J. Pauza, K. Pezaz, T. Sun, A.D. Rollett, Keyhole threshold and morphology in laser melting revealed by ultrahigh-speed x-ray imaging, *Science* (80-. ) 363 (2019) 849–852, <https://doi.org/10.1126/science.aav4687>.
- [18] S.A. Khairallah, A.A. Martin, J.R.I. Lee, G. Guss, N.P. Calta, J.A. Hammons, M.H. Nielsen, K. Chaput, E. Schwalbach, M.N. Shah, M.G. Chapman, T.M. Willey, A.M. Rubenchik, A.T. Anderson, Y.M. Wang, M.J. Matthews, W.E. King, Controlling interdependent meso-nanosecond dynamics and defect generation in metal 3D printing, *Science* (80-. ) 368 (2020) 660–665, <https://doi.org/10.1126/science.aay7830>.
- [19] H. Gong, K. Rafi, H. Gu, G.D. Janaki Ram, T. Starr, B. Stucker, Influence of defects on mechanical properties of Ti-6Al-4V components produced by selective laser melting and electron beam melting, *Mater. Des.* 86 (2015) 545–554, <https://doi.org/10.1016/j.matdes.2015.07.147>.
- [20] E. Wycisk, A. Solbach, S. Siddique, D. Herzog, F. Walther, C. Emmelmann, Effects of defects in laser additive manufactured Ti-6Al-4V on fatigue properties, *Phys. Procedia*, Elsevier B.V 2014, pp. 371–378, <https://doi.org/10.1016/j.phpro.2014.08.120>.
- [21] M. Tang, P.C. Pistorius, J.L. Beuth, Prediction of lack-of-fusion porosity for powder bed fusion, *Addit. Manuf.* 14 (2017) 39–48, <https://doi.org/10.1016/j.addma.2016.12.001>.
- [22] J. Elambasseril, S.L. Lu, Y.P. Ning, N. Liu, J. Wang, M. Brandt, H.P. Tang, M. Qian, 3D characterization of defects in deep-powder-bed manufactured Ti-6Al-4V and their influence on tensile properties, *Mater. Sci. Eng. A* 761 (2019), 138031, <https://doi.org/10.1016/j.msea.2019.138031>.
- [23] M. Hamidi Nasab, S. Romano, D. Gastaldi, S. Beretta, M. Vedani, Combined effect of surface anomalies and volumetric defects on fatigue assessment of AISI7Mg fabricated via laser powder bed fusion, *Addit. Manuf.* (2019), 100918, <https://doi.org/10.1016/j.addma.2019.100918>.
- [24] S. Razavi, G. Bordonaro, P. Ferro, J. Torgersen, F. Berto, Porosity effect on tensile behavior of Ti-6Al-4V specimens produced by laser engineered net shaping technology, *Proc. Inst. Mech. Eng. Part C J. Mech. Eng. Sci.* (2018), 095440621881338, <https://doi.org/10.1177/0954406218813384>.
- [25] S. Razavi, G. Bordonaro, P. Ferro, J. Torgersen, F. Berto, Fatigue behavior of porous Ti-6Al-4V made by laser-engineered net shaping, *Materials* (Basel) 11 (2018) 284, <https://doi.org/10.3390/ma11020284>.
- [26] I. Yadroitsev, P. Krakhmalev, I. Yadroitsava, A. Du Plessis, Qualification of Ti6Al4V ELI alloy produced by laser powder bed fusion for biomedical applications, *JOM* 70 (2018) 372–377, <https://doi.org/10.1007/s11837-017-2655-5>.
- [27] S.M.J. Razavi, F. Berto, Directed energy deposition versus wrought Ti-6Al-4V: a comparison of microstructure, fatigue behavior, and notch sensitivity, *Adv. Eng. Mater.* 21 (2019), 1900220, <https://doi.org/10.1002/adem.201900220>.
- [28] M. Qian, W. Xu, M. Brandt, H.P. Tang, Additive manufacturing and postprocessing of Ti-6Al-4V for superior mechanical properties, *MRS Bull.* 41 (2016) 775–784, <https://doi.org/10.1557/mrs.2016.215>.
- [29] S. Liu, Y.C. Shin, Additive manufacturing of Ti6Al4V alloy: a review, *Mater. Des.* 164 (2019), 107552, <https://doi.org/10.1016/j.matdes.2018.107552>.
- [30] L. Ladani, Local and global mechanical behavior and microstructure of Ti6Al4V parts built using Electron beam melting technology, *Metall. Mater. Trans. A Phys. Metall. Mater. Sci.* 46 (2015) 3835–3841, <https://doi.org/10.1007/s11661-015-2965-6>.
- [31] L. Ladani, J. Razmi, S.F. Choudhury, Mechanical anisotropy and strain rate dependency behavior of Ti6Al4V produced using E-beam additive fabrication, *J. Eng. Mater. Technol. Trans. ASME*. 136 (2014) <https://doi.org/10.1115/1.4027729>.
- [32] A.M. Beese, B.E. Carroll, Review of mechanical properties of Ti-6Al-4V made by laser-based additive manufacturing using powder feedstock, *JOM* 68 (2016) 724–734, <https://doi.org/10.1007/s11837-015-1759-z>.
- [33] M. Grasso, B.M. Colosimo, Process defects and in situ monitoring methods in metal powder bed fusion: a review, *Meas. Sci. Technol.* 28 (2017), 044005, <https://doi.org/10.1088/1361-6501/AA5C4F>.
- [34] S.K. Everton, M. Hirsch, P.I. Stavroulakis, R.K. Leach, A.T. Clare, Review of in-situ process monitoring and in-situ metrology for metal additive manufacturing, *Mater. Des.* 95 (2016) 431–445, <https://doi.org/10.1016/j.matdes.2016.01.099>.
- [35] A. Du Plessis, I. Yadroitsev, I. Yadroitsava, S.G. Le Roux, X-ray microcomputed tomography in additive manufacturing: a review of the current technology and applications, *3D print. Addit. Manuf.* 5 (2018) 227–247, <https://doi.org/10.1089/3dp.2018.0060>.
- [36] S. Romano, A. Brandão, J. Gumpinger, M. Gschweilt, S. Beretta, Qualification of AM parts: extreme value statistics applied to tomographic measurements, *Mater. Des.* 131 (2017) 32–48, <https://doi.org/10.1016/j.matdes.2017.05.091>.
- [37] A. Thompson, I. Maskery, R.K. Leach, X-ray computed tomography for additive manufacturing: a review, *Meas. Sci. Technol.* 27 (2016), 072001, <https://doi.org/10.1088/0957-0233/27/7/072001>.
- [38] M. Ahlfors, F. Bahbou, A. Eklund, HIP for AM - optimized material properties by HIP, *Mater. Res. Proc.* 10 (2019) 1–10, <https://doi.org/10.21741/9781644900031-1>.
- [39] A. du Plessis, E. Macdonald, Hot isostatic pressing in metal additive manufacturing: X-ray tomography reveals details of pore closure, *Addit. Manuf.* 34 (2020), 101191, <https://doi.org/10.1016/j.addma.2020.101191>.
- [40] M. Seifi, A.A. Salem, D.P. Satko, U. Ackelid, S.L. Semiatin, J.J. Lewandowski, Effects of HIP on microstructural heterogeneity, defect distribution and mechanical properties of additively manufactured EBM Ti-48Al-2Cr-2Nb, *J. Alloys Compd.* 729 (2017) 1118–1135, <https://doi.org/10.1016/j.jallcom.2017.09.163>.
- [41] A. Yadollahi, N. Shamsaei, Additive manufacturing of fatigue resistant materials: challenges and opportunities, *Int. J. Fatigue* 98 (2017) 14–31, <https://doi.org/10.1016/j.ijfatigue.2017.01.001>.
- [42] H. Masuo, Y. Tanaka, S. Morokoshi, H. Yagura, T. Uchida, Y. Yamamoto, Y. Murakami, Effects of defects, surface roughness and HIP on fatigue strength of Ti-6Al-4V manufactured by additive manufacturing, *Procedia Struct. Integr.* 7 (2017) 19–26, <https://doi.org/10.1016/j.prostr.2017.11.055>.
- [43] M. Leary, Design for Additive Manufacturing, (n.d).
- [44] A. du Plessis, C. Broeckhoven, I. Yadroitsava, I. Yadroitsev, C.H. Hands, R. Kunju, D. Bhate, Beautiful and functional: a review of biomimetic design in additive manufacturing, *Addit. Manuf.* 27 (2019) 408–427, <https://doi.org/10.1016/j.addma.2019.03.033>.
- [45] D. Bhate, C. Penick, L. Ferry, C. Lee, D. Bhate, C.A. Penick, L.A. Ferry, C. Lee, Classification and selection of cellular materials in mechanical design: engineering and biomimetic approaches, *Designs* 3 (2019) 19, <https://doi.org/10.3390/designs3010019>.
- [46] L.E. Murr, Strategies for creating living, additively manufactured, open-cellular metal and alloy implants by promoting osseointegration, osteoinduction and vascularization: an overview, *J. Mater. Sci. Technol.* 35 (2019) 231–241, <https://doi.org/10.1016/j.jmst.2018.09.003>.
- [47] L.E. Murr, Open-cellular metal implant design and fabrication for biomechanical compatibility with bone using electron beam melting, *J. Mech. Behav. Biomed. Mater.* 76 (2017) 164–177, <https://doi.org/10.1016/j.jmbbm.2017.02.019>.
- [48] X.P. Tan, Y.J. Tan, C.S.L. Chow, S.B. Tor, W.Y. Yeong, Metallic powder-bed based 3D printing of cellular scaffolds for orthopaedic implants: a state-of-the-art review on manufacturing, topological design, mechanical properties and biocompatibility, *Mater. Sci. Eng. C* 76 (2017) 1328–1343, <https://doi.org/10.1016/j.msec.2017.02.094>.
- [49] X. Wang, S. Xu, S. Zhou, W. Xu, M. Leary, P. Choong, M. Qian, M. Brandt, Y.M. Xie, Topological design and additive manufacturing of porous metals for bone scaffolds and orthopaedic implants: a review, *Biomaterials* 83 (2016) 127–141, <https://doi.org/10.1016/j.biomaterials.2016.01.012>.
- [50] A.A. Zadpoor, Mechanical performance of additively manufactured meta-biomaterials, *Acta Biomater.* 85 (2019) 41–59, <https://doi.org/10.1016/j.actbio.2018.12.038>.

- [51] T. Maconachie, M. Leary, B. Lozanovski, X. Zhang, M. Qian, O. Faruque, M. Brandt, SLM lattice structures: properties, performance, applications and challenges, *Mater. Des.* 183 (2019), 108137. <https://doi.org/10.1016/j.matdes.2019.108137>.
- [52] A.M. Vilarde, A. Takezawa, A. du Plessis, N. Takata, P. Krakhmalev, M. Kobashi, I. Yadroitsava, I. Yadroitsev, Topology optimization and characterization of Ti6Al4V ELI cellular lattice structures by laser powder bed fusion for biomedical applications, *Mater. Sci. Eng. A* 766 (2019), 138330. <https://doi.org/10.1016/j.msea.2019.138330>.
- [53] A. Du Plessis, D.-P. Kouprianoff, I. Yadroitsava, I. Yadroitsev, A. Du Plessis, D.-P. Kouprianoff, I. Yadroitsava, I. Yadroitsev, Mechanical properties and in situ deformation imaging of microlattices manufactured by laser based powder bed fusion, *Mater.* 11 (2018) 1663, 11 (2018) 1663 <https://doi.org/10.3390/MA11091663>.
- [54] C.N. Kelly, J. Francovich, S. Julmi, D. Safranski, R.E. Guldborg, H.J. Maier, K. Gall, Fatigue behavior of As-built selective laser melted titanium scaffolds with sheet-based gyroid microarchitecture for bone tissue engineering, *Acta Biomater.* 94 (2019) 610–626, <https://doi.org/10.1016/j.actbio.2019.05.046>.
- [55] A. du Plessis, Effects of process parameters on porosity in laser powder bed fusion revealed by X-ray tomography, *Addit. Manuf.* 30 (2019), 100871. <https://doi.org/10.1016/j.addma.2019.100871>.
- [56] K.G. Prashanth, S. Scudino, T. Maity, J. Das, J. Eckert, Is the energy density a reliable parameter for materials synthesis by selective laser melting? *Mater. Res. Lett.* 5 (2017) 386–390, <https://doi.org/10.1080/21663831.2017.1299808>.
- [57] C. Cai, B. Song, P. Xue, Q. Wei, J.M. Wu, W. Li, Y. Shi, Effect of hot isostatic pressing procedure on performance of Ti6Al4V: surface qualities, microstructure and mechanical properties, *J. Alloys Compd.* 686 (2016) 55–63, <https://doi.org/10.1016/j.jallcom.2016.05.280>.
- [58] F.S.L. Bobbert, K. Lietaert, A.A. Eftekhari, B. Pouran, S.M. Ahmadi, H. Weinans, A.A. Zadpoor, Additively manufactured metallic porous biomaterials based on minimal surfaces: a unique combination of topological, mechanical, and mass transport properties, *Acta Biomater.* 53 (2017) 572–584, <https://doi.org/10.1016/j.actbio.2017.02.024>.
- [59] T. Persenot, A. Burr, R. Dendievel, J.Y. Buffière, E. Maire, J. Lachambre, G. Martin, Fatigue performances of chemically etched thin struts built by selective electron beam melting: experiments and predictions, *Materialia* 9 (2020), 100589. <https://doi.org/10.1016/j.mtla.2020.100589>.